ALGORITHM THEORETICAL BASIS DOCUMENT (ATBD):

NEON ELEVATION (SLOPE AND ASPECT)

PREPARED BY	ORGANIZATION	DATE
Tristan Goulden	AOP	05/29/2019

APPROVALS	ORGANIZATION	APPROVAL DATE
David Barlow	SYS	06/11/2019

RELEASED BY	ORGANIZATION	RELEASE DATE
Anne Balsley	CM	07/01/2019

See configuration management system for approval history.

Change Record

REVISION	DATE	ECO #	DESCRIPTION OF CHANGE
A	07/01/2019	ECO-06170	Initial Release

TABLE OF CONTENTS

LIST OF TABLES AND FIGURES

1   DESCRIPTION

1.1   Purpose

This document details the algorithms used for creating the NEON Level 3 slope and aspect data product (NEON.DOM.SIT.DP3.30025) from Level 1 data, and ancillary data (such as calibration data), obtained via instrumental measurements made by the Light Detection and Ranging (LiDAR) sensor on the Airborne Observation Platform (AOP). It includes a detailed discussion of measurement theory and implementation, appropriate theoretical background, data product provenance, quality assurance and control methods used, approximations and/or assumptions made, and a detailed exposition of uncertainty resulting in a cumulative reported uncertainty for this product.

1.2   Scope

This document describes the theoretical background and entire algorithmic process for creating NEON.DOM.SIT.DP2.30025 from input data. It does not provide computational implementation details, except for cases where these stem directly from algorithmic choices explained here.

2   RELATED DOCUMENTS, ACRONYMS AND VARIABLE NOMENCLATURE

2.1   Applicable Documents

AD[01]	NEON.DOC.000001	NEON Observatory Design (NOD) Requirements
AD[02]	NEON.DOC.002652	NEON Level 1, Level 2 and Level 3 Data Products Catalog
AD[03]	NEON.DOC.002293	NEON Discrete LiDAR datum reconciliation report
AD[04]	NEON.DOC.002649	NEON configured site list

2.2   Reference Documents

RD[01]	NEON.DOC.000008	NEON Acronym List
RD[02]	NEON.DOC.000243	NEON Glossary of Terms
RD[03]	NEON.DOC.001292	NEON elevation Algorithm Theoretical Basis Document
RD[04]	NEON.DOC.001984	AOP flight plan boundaries design
RD[05]	NEON.DOC.005011	NEON Coordinate Systems Specification
RD[06]	NEON.DOC.001292 document	NEON L0-to-L1 discrete return lidar algorithm theoretical basis
RD[07]	NEON.DOC.002890	NEON AOP Level 0 quality checks

2.3   Acronyms

Acronym	Explanation
DTM	Digital Terrain model
DSM	Digital Surface model
DEM	Digital Elevation Model
ITRF00	International Terrestrial Reference Frame 2000
UTM	Universal Transverse Mercator
TIFF	Tagged Image File Format
AOP	Airborne Observation Platform
FBO	Fixed Base Operator
PPM	pulses per square meter

3   DATA PRODUCT DESCRIPTION

3.1   Variables Reported

The products supplied through NEON.DOM.SIT.DP3.30025 include a slope map and aspect map, both in raster format. Slope and aspect maps are derived from the DTM (Digital Terrain Model), which includes only elevations which relate to the physical terrain surface (see RD[03]). Raster maps for the slope and aspect are reported with horizontal reference to the ITRF00 datum, projected to the Universal Transverse Mercator (UTM) mapping frame in accordance with RD[05]. Slope is determined as the angle between a plane tangential to the local

terrain surface and a plane tangential to the local Geoid12A surface, reported in degrees. Aspect is the direction of the steepest slope, given in degrees referenced to grid north. The slope and aspect rasters are divided into a set of 1 km by 1 km tiles, which have corners spatially referenced to an even kilometer. The product is stored in a GeoTIFF format in accordance with the GeoTIFF specification (Ritter et al., 2000).

3.2 Input Dependencies

The creation of the slope and aspect rasters requires only an input DTM. Procedures for creating a DTM from L1 data can be found in RD[03].

3.3 Product Instances

The NEON data products produced directly from these algorithms are summarized in Table 1.

Table 1 - Data products generated by algorithms described within this ATBD

Data product identification	Data product name
NEON.DOM.SITE.DP3.30025	Slope
NEON.DOM.SITE.DP3.30025	Aspect

3.4 Temporal Resolution and Extent

The slope and aspect products will include data collected during acquisition of a single core, re-locatable or aquatic site by the AOP. Depending on external variables such as weather, transit time to the site FBO (Fixed Based Operator), and total area of the priority 1 flight box (see RD[04]), the temporal resolution of a single acquisition of L0 LiDAR information could range from a single flight (4 hrs.) to several flights acquired over multiple days. Generally, due to the peak greenness constraint of AOP data acquisition (site at > 90% peak greenness value), and the requirement that all sites are to be flown annually, the total potential time to acquire a site will have a limit which defines the largest temporal resolution for a single acquisition. Details defining the total amount of potential time dedicated to a single site acquisition are given in RD[04]. As the NEON AOP payload is scheduled to repeat each NEON site on an annual basis, the temporal resolution of multiple acquisitions will be one year.

3.5 Spatial Resolution and Extent

The slope and aspect are created from a 1 m spatial resolution raster DTM, and shall maintain the 1 m spatial resolution. The planned spatial extent of the slope and aspect maps will relate to the definition of the AOP flight box for each individual site (RD[04]). It is intended that a minimum of 80% of the priority 1 flight box and 95% of the tower airshed will be acquired each year (RD[07]). As discussed in Section 3.4, the actual acquired area could vary depending on external conditions encountered during the flight. Ultimately, the

flight schedule as defined in RD[04] shall supersede the percent coverage requirement. Therefore, the actual acquired spatial extent may vary annually.

4   SCIENTIFIC CONTEXT

Slope and aspect are first-order derivatives of the three dimensional terrain surface. Let the terrain elevation (z) to be theoretically described as a continuous and differentiable function of the form

$$z = f(x, y) \tag{1}$$

where x, y are horizontal coordinates in the east-west direction and north-south direction respectively. The derivative of z at an given x and y can be described with a vector, generally referred to as the gradient (Δ), whose components are the partial derivatives of z with respect to x and y. Slope equates to the magnitude of Δ, and aspect its direction in the horizontal plane. It follows that, in mathematical notation, slope and aspect can be written as (Hunter & Goodchild, 1997):

$$Slope = \left[\left(\frac{\partial z}{\partial x} \right)^2 + \left(\frac{\partial z}{\partial y} \right)^2 \right]^{1/2} \tag{2}$$

$$spect = arctan\left(-\frac{\partial z}{\partial y} \middle/ \frac{\partial z}{\partial x} \right) \tag{3}$$

Since we have knowledge of only a discrete representation of $f(x, y)$ through the DTM, and not its true continuous mathematical form, the derivative must be estimated using finite difference methods. Typically, finite difference methods will consider the derivative at any given cell in the DTM and utilize information from a limited neighborhood surrounding the DTM grid cell (see Section 4.2).

Slope and aspect provide valuable information on the terrain structure which can be ingested as spatial data layers in ecosystem models. For example, slope is often used in hydrological analysis for predicting overland and subsurface flow velocity and the erosive potential of overland and channel flow. These physical processes are important to characterizing the eco-system as they influence the incidence of particle detachment which governs the terrain shape and influences to hydrological, geomorphological and ecological processes (Moore et al., 1993). Aspect provides a metric for determining the topological relationship between streams channels, assigning stream orders, and defining watershed boundaries (Jenson & Domingue, 1988). Additionally, both slope and aspect are predictors of incident solar radiation which can drive certain ecological and physical landscape processes (Gates, 2012) of interest such as evapotranspiration and snow-melt. Therefore, consideration and ingestion of slope and aspect into spatially driven models of landscape processes will allow for enhanced spatial predictability of phenomena internal and external to the landscape.
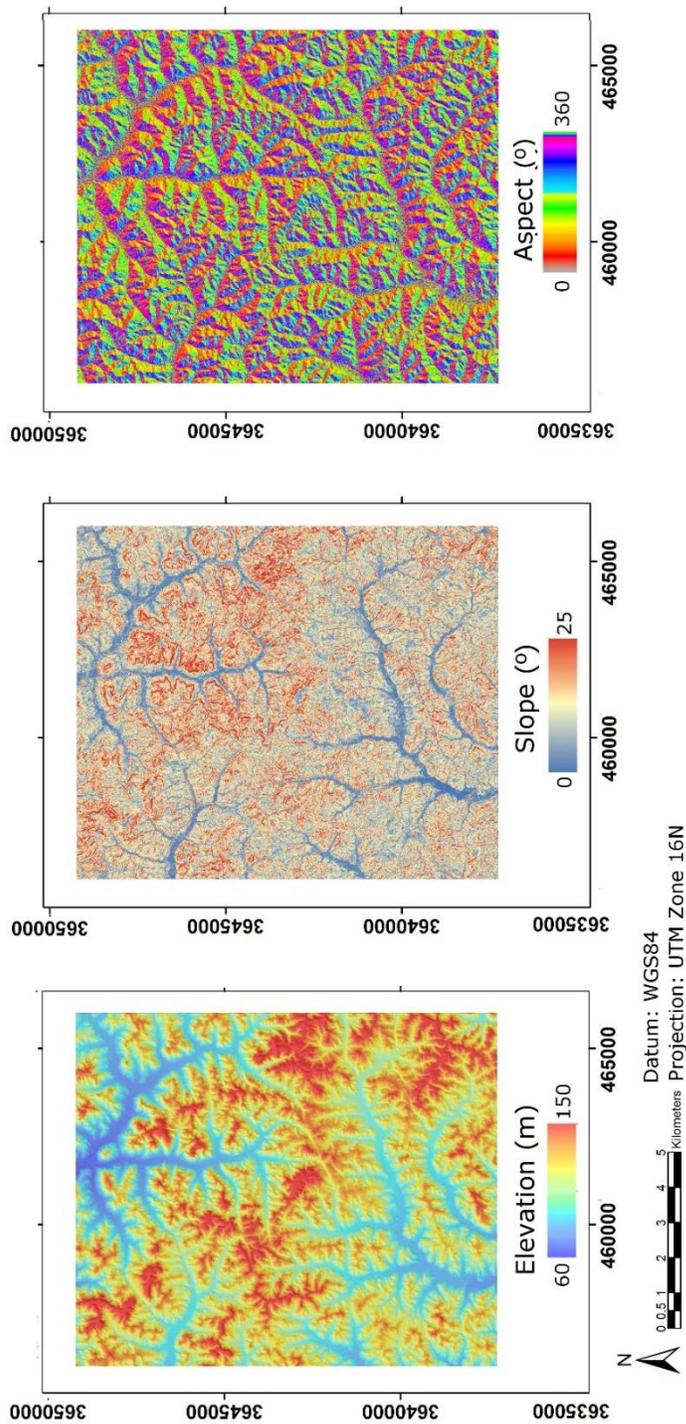
Figure 1 - DTM (elevation), slope and aspect for a portion of the NEON LiDAR survey over Talladega National Forest

4.1 Theory of Measurement

The slope and aspect maps are derived from the DTM (see RD[03]). The DTM is an L3 product derived from the LiDAR point cloud, an L1 product (see RD[06]). As detailed in RD[06], the LiDAR sensor measures three-dimensional coordinates of the terrain and surface features. Surface features such as buildings and trees can be filtered, leaving only ground returns. The ground returns are interpolated into a regularly spaced grid of elevation values (DTM). The elevation values in the DTM are used to determine the slope and aspect at each individual cell in the raster.

4.2 Theory of Algorithm

The equation implemented by NEON for calculating slope and aspect from a terrain ∇ was first provided by Horn (1981). The Horn (1981) algorithm is a third-order finite difference approximation of the terrain derivative which considers the 3 x 3 neighborhood surrounding each grid cell and directly calculates the north-south (∇_y) and east-west (∇_x) components of ∇. The slope and aspect are then extracted from ∇_y and ∇_x. Let each elevation in the DTM grid be represented by $z_{i,j}$, where i and j represent the east-west and north-south horizontal indexes of the grid cells respectively, then

$$\nabla_x = \left[\left(z_{i+1,j+1} + 2z_{i+1,j} + z_{i+1,j-1}\right) - \left(z_{i-1,j+1} + 2z_{i-1,j} + z_{i-1,j-1}\right)\right]/8\Delta_x \qquad (4)$$

$$\nabla_y = \left[\left(z_{i+1,j+1} + 2z_{i,j+1} + z_{i-1,j+1}\right) - \left(z_{i-1,j-1} + 2z_{i,j-1} + z_{i+1,j-1}\right)\right]/8\Delta_x \qquad (5)$$

where Δx is the cell size of the DTM (1 m for NEON DTMs). The slope (in radians) can then be calculated as

$$Slope = \sqrt{\nabla_x^2 + \nabla_y^2} \qquad (6)$$

and the aspect (in radians) can be calculated as

$$Aspect = \text{atan}\left(-\frac{\nabla_y}{\nabla_x}\right) \qquad (7)$$

care must be taken in the calculation of *Aspect* to ensure the appropriate azimuthal direction is produced since the arctan function is constrained to a result between -90° and 90°, and we desire an azimuthal direction between 0° and 360° with reference to grid north. To ensure the correct azimuthal direction is produced, the correct quadrant of the direction, based on the signs of both ∇_x and ∇_y must be selected and the appropriate offset applied. Alternatively, the arctan 2 function (http://www.mathworks.com/help/matlab/ref/atan2.html) can be exploited as follows

$$Aspect = \text{atan2}\left(\nabla_x, \nabla_y\right) \qquad (8)$$

with the following logic (ESRI, 2015), after conversion to degrees:

$$\textbf{if } Aspect \quad < 0$$

$$Aspect_{Az} = 90 - Aspect$$

$$\textbf{else if } Aspect \quad > 90.0$$

$$Aspect_{Az} = 360 - Aspect + 90$$

$$\textbf{else}$$

$$Aspect_{Az} = 90 - Aspect$$

where $Aspect_{Az}$ is the final aspect with the appropriate azimuthal direction ($0°$ to $360°$).

4.2.1 Pre-Processing

As described in RD[03], the original DTM is created with the TIN (Triangular Irregular Network) interpolation method. A deficiency of the TIN interpolation method is that the available redundancy of multiple LiDAR observations within a single DTM grid cell are not exploited to reduce noise through averaging. This can propagate unnecessary uncertainty into the slope and aspect rasters, which are sensitive to high frequency noise, especially in flat terrain and at high spatial resolutions. To reduce the uncertainty in the slope and aspect maps, the original DTM is filtered with a morphological averaging filter using a 3 x 3 neighborhood window. Within the 3 x 3 moving window, all cells are given equal weight to the averaged result. To demonstrate the improvement after application of the morphological averaging filter, internal testing at NEON over the Boulder runway using nominal flight parameters (100 kHz PRF, 1000 m AGL flight altitude) was conducted. Results show that the relatively smooth runway surface has a high level of noise in the slope results if the morphological averaging filter has not been applied to the DTM. The slope becomes more consistent along the runway when determined from the DTM with the 3 x 3 morphological averaging filter applied (**Figure 2**). Although not shown in **Figure 2**, similar results were obtained for aspect. Prior to creation of the rasters, the input files also contain a buffer of 20 m on each edge. This allows the triangulation to occur on smaller subsets of data without creating artifacts at tile edges. The processing of the DTM, filtered DTM, slope and aspect are all conducted with the buffer. Once complete, the buffer is removed from the tiled rasters.
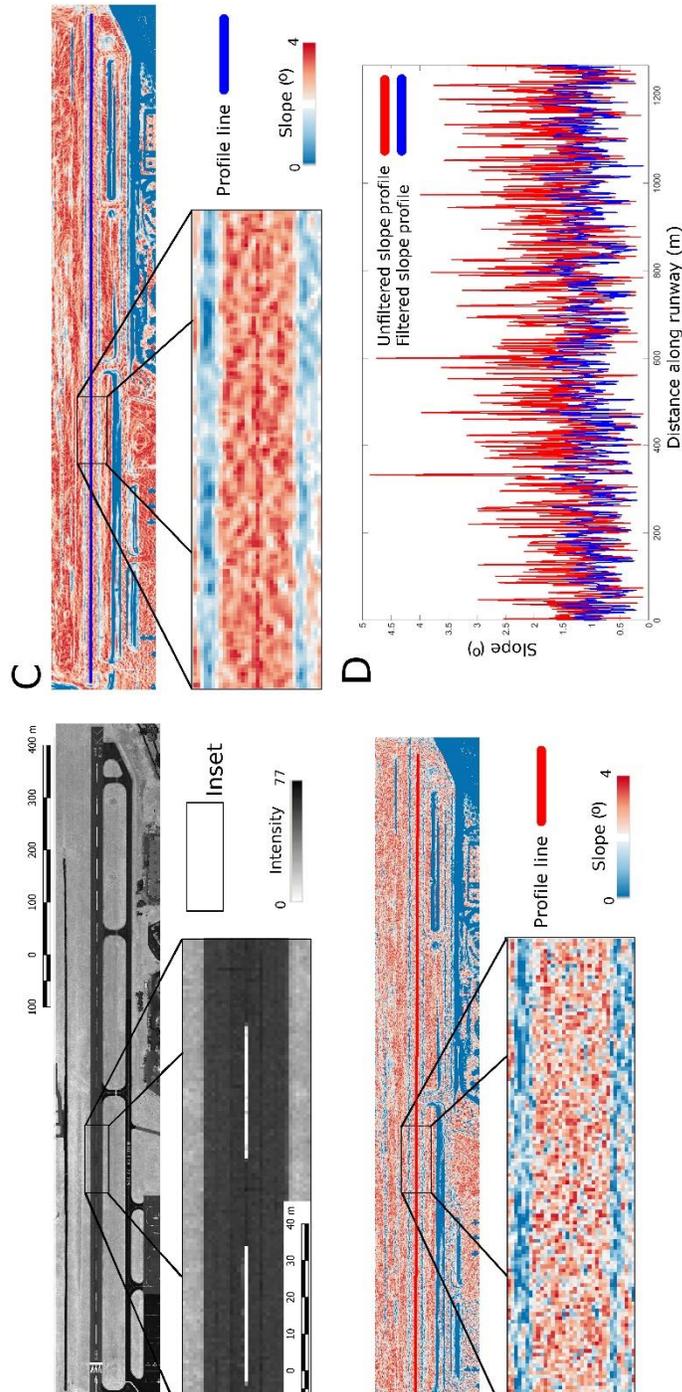
Figure 2 - Noise reduction in slope calculation after applying morphological averaging filter to the DTM. Panel A: Intensity image of flight line, including low slope smooth runway surface, panel B: Slope results over the runway after averaging on the DTM has been applied, panel C: slope results over the runway after averaging has occurred on the DTM, panel D: slope results along profile lines of slope results from the averaged and non-averaged DTMs

5   ALGORITHM IMPLEMENTATION

The processing of the DTM into the slope and aspect products is achieved through the steps outlined in this section (**Figure 3**). The algorithm for slope and aspect calculations is implemented through multiple interconnected Matlab functions which automate the algorithm. The process is dependent on only the existence of completed DTM tiles. Details into the algorithm which creates the DTM tiles can be found in RD[03].
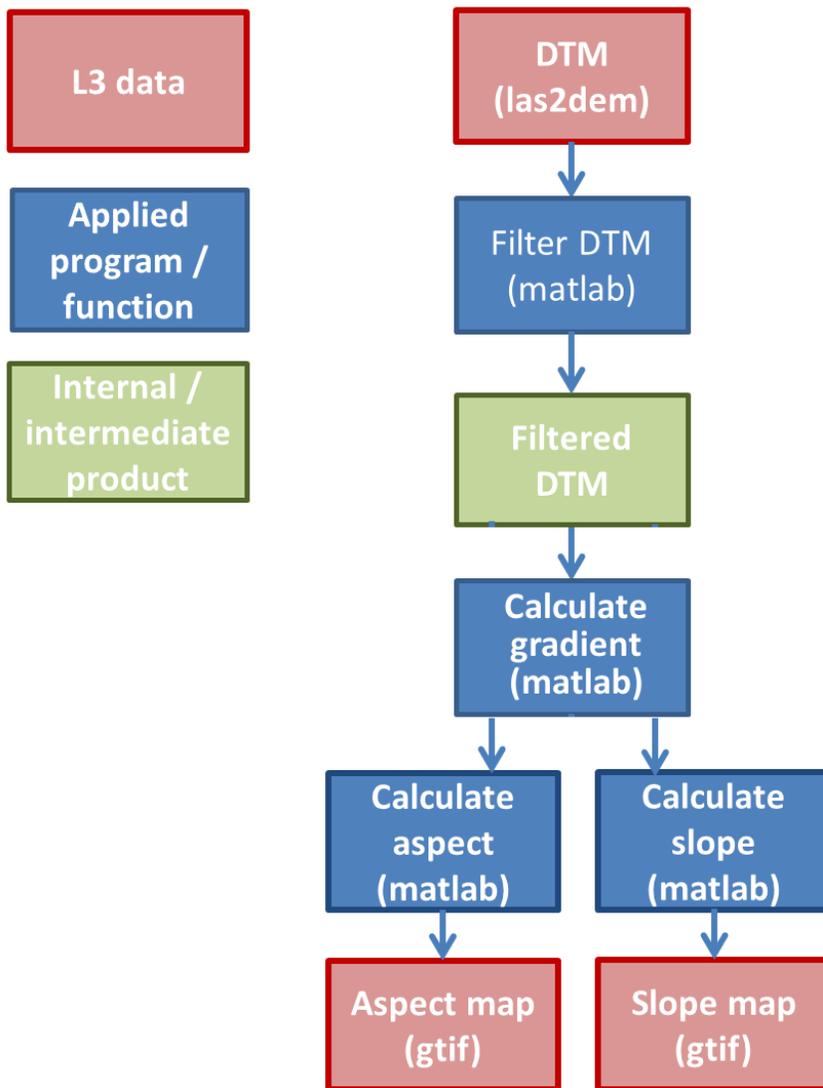
Figure 3 - Flowchart summarizing slope and aspect creation

Step 1:

DTM tiles are filtered with a moving 3 x 3 moving window as described in Section 4.2.1

Input:

1. all DTM tiles in gtif format

2. flag which indicates buffer size (20 m) for each tile

Output: Filtered DTM tiles in Geotiff format

Functions used: filter_DTM_create_slope_aspect.m

Step 2:

Calculate slope according to Equation (6)

Input: Filtered DTM tiles with buffer from Step 1

Output: Tiled slope maps in Geotiff format with buffer removed

Functions used: filter_DTM_create_slope_aspect.m

Step 3:

Calculate aspect according to Equation (8)

Input: Filtered DTM tiles with buffer from Step 1

Output: Tiled aspect maps in Geotiff format with buffer removed

Functions used: filter_DTM_create_slope_aspect.m

6   UNCERTAINTY

To understand the uncertainty in the slope and aspect, error sources in the DTM must be first considered. Error sources in the DTM are relevant because slope and aspect are derived directly from the DTM (see Section 5). Therefore, any source of uncertainty in the DTM will propagate through to the slope and aspect products. As described in RD[03], Fisher and Tate (2006) identify three primary categories of uncertainty in DTMs:

1. errors related to the sensor or instrument used to acquire the data.

2. errors related to the processing and interpolation of the data.

3. errors introduced by the structure of the terrain / landscape

Quantifying the uncertainty in slope and aspect through category 1 is straightforward, as LiDAR system instrument errors can be propagated through the DTM and subsequently to the slope and aspect products. The propagation of instrument errors from the DTM to slope and aspect can be accomplished through direct functional modeling as in Florinsky (1998), or through simulation (Hunter & Goodchild, 1997; Raaflaub & Collins, 2006; Goulden et al., 2016). Direct functional modeling of uncertainty eases processing time as uncertainty values are the result of the computation of a single equation. Simulation requires significantly more processing time, but avoids the derivation of an uncertainty equation, which can be complicated by non-linear behavior of the func- tion, or correlation between variables. Raaflaub and Collins (2006) note that due to the non-linear nature of several slope and aspect calculation methods, simulation provides a more practical approach than direct functional modeling. The uncertainty in slope and aspect calculations currently implemented at NEON through the Horn (1981) method can be determined through a direct functional relationship (see Florinsky (1998)), however; the simulation approach is implemented. Simulation is selected over direct functional modeling because it allows updated slope and aspect formulations to be applied in the future without the need to derive updated uncertainty equations, and allows the flexibility of the future implementation of slope and aspect calculations which may not be well-conditioned for direct functional modeling. The simulation process is unaffected by the underlying equation used to calculate slope and aspect, allowing for a robust implementation of the algorithm in an automated processing chain.

Uncertainty in slope and aspect introduced through category two, processing and interpolation of the data, can be divided into three additional sub-categories:

(a) selection of the grid cell size

(b) selection of the algorithm

(c) filtering errors in the LiDAR point cloud

Analysis into the uncertainty due to varying the grid cell size on slope and aspect maps (category 2a) has shown that the mean slope determined from a DTM will increase as cell size decreases (Chang & Tsai, 1991; Zhang & Montgomery, 1994; Kienzle, 2004; Hopkinson et al., 2010), due to the ability of smaller grid cells to represent minor topographic variations in the landscape. Aspect has shown sensitivity to grid cell size, however, the relationship does not present in a systematic fashion as does slope (Kienzle, 2004; Erskine et al., 2006; Hopkinson et al., 2010). The nominal choice of 1 m spatial resolution slope and aspect maps produced at NEON was made to enable representation of fine scale variations in the terrain, however, the influence of noise present in the DTM (due to category one) will more severely affect results at fine scales. As grid cell sizes are reduced, any noise in the DTM will propagate more heavily into the slope and aspect calculations (Erskine et al., 2006). Therefore, a compromise exists between maintaining a spatial scale which accurately represents the structure of the topography while also minimizing the influence of instrument error (from category one). If users determine that the level of noise in the 1 m slope and aspect products is

unacceptable, they may wish to apply additional smoothing to the DTM and re-calculate slope, apply smoothing routines directly to the slope and aspect maps, or create slope and aspect with a larger grid cell size. However, applying such approaches will further reduce the ability to detect fine-scale variations in the topography thorough the slope and aspect maps and any associated phenomena occurring at these scales.

Category 2b describes uncertainty due to the selection of the particular algorithm used to calculate slope. Previ- ous investigations have shown that the second-order finite difference algorithm by Zevenbergen and Thorne (1987) as well as the third-order finite difference algorithm of Horn (1981) have produced the most accurate results of available slope and aspect equations (Jones, 1998; Skidmore, 1989). Burrough (1998) suggested that the second-order finite difference method was more accurate in smooth terrain while the third-order finite difference method was more ac- curate in rough or textured terrain. However, neither Jones (1998) or Skidmore (1989) analyzed high resolution LiDAR data. In a study that included multiple resolution DEMs and included a high resolution DEM (1 m), Warren et al. (2004) found that DEM resolution had little influence on the overall accuracy of the method selected, indicating results from Jones (1998) and Skidmore (1989) remain relevant to high resolution DTMs produced from LiDAR. Therefore, it is expected that the algorithm selection has minor effect to the overall uncertainty.

Category 2c describes the uncertainty introduced through incorrect classification / filtering of the LiDAR point cloud. This source of uncertainty is discussed in greater detail in Section 6.1 of RD[03]. In summary, the LiDAR point cloud classification routine can often misclassify ground points as non-ground and vice versa. This can result in anomalous features in the DTM which will yield incorrect estimates of slope and aspect. For example, **Figure 5** of RD[03] shows the highest elevation areas of steep mountain peaks incorrectly classified as non-ground points, leaving them absent from the DTM. As a result, large gaps form in the DTM and are interpolated across and filled by the TIN algorithm. In these sections the slope and aspect will be incorrect. A similar situation can also occur in areas where dense vegetation pre- vents LiDAR pulses from reaching the true ground surface. Although this may not be a result of point misclassification, the effect on the slope and aspect maps is similar. These areas can be easily identified visually because there will not be any variability in the slope and aspect results between adjacent cells. If non-ground points are incorrectly classified as ground, this could have the opposite result, introducing incorrect, but highly variable slope and aspect results. Al- though this may present one of the largest sources of uncertainty in the slope and aspect maps, it is difficult to identify and quantify errors in the absence of field observations to confirm misclassification errors. Therefore, visual inspections of the data are required to identify areas suspected of suffering from misclassifications. By request, users can obtain raster images of the DTM which provide the interpolation distance applied in the DTM creation process, and can provide insight into areas with sparse ground points and increased uncertainty.

Errors introduced through category three, the structure of the terrain, are relevant when implementing the slope and aspect as data layers into spatially driven models. It has been suggested that to minimize uncertainty in modeled results, the DTMs used in spatial models should correspond to the natural scale of the terrain (Quinn et al., 1991; Zhang & Montgomery, 1994; Hutchinson & Gallant, 2000; McMaster, 2002; Goulden et al., 2014). For example, research into spatially based hydrological models has concluded that 10 m resolution is normally sufficient for watershed-scale hydrological modeling (Zhang & Montgomery, 1994).

However, it has also been identified that depending on the width of stream channels, channel processes may require higher resolutions DTMs (Goulden et al., 2014). Therefore, consideration should be given to the correspondence between the DTM spatial resolution and the desired scale of the modeled variable of interest. Additionally, Warren et al. (2004) noted that models for simulating erosive potential due to slope are often performed on field scale plots with highly accurate measurements of slope. The models are then transferred to a GIS environment where a large variation in slopes from DTMs are applied and may not be valid. For example, it has been observed that the application of the field-derived empirical relationships of the RUSLE (revised universal soil loss equation) in a GIS based model (SWAT, Soil and Water Assessment Tool) with high resolution DTMs can prohibit a realistic parameterization of soil erosion models (Goulden, Jamieson, et al., 2014). Users should exercise caution, and consider the source of relationships inherent to the model, when applying the 1 m resolution slope and aspect maps as data layers into spatially driven models to ensure scale related uncertainty is minimized.

6.1   Analysis of Uncertainty

Due to the fact that processing and interpolation errors (category 2) and errors due to the structure of the landscape (category 3) are insignificant or not directly quantifiable, focus on the analysis of uncertainty is placed on propagat- ing errors from category one, errors related to the instrument. As discussed in Section 6, the preferred method for quantifying uncertainty in slope and aspect is through simulation. Previous simulation approaches used to quantify uncertainty in slope and aspect have introduced DTM errors through auto-correlated random fields of error, and then executed Monte Carlo simulations to quantify uncertainty (Hunter & Goodchild, 1996; Holmes et al., 2000; Oksanen & Sarjakoski, 2005; Wechsler & Kroll, 2006; Raaflaub & Collins, 2006; Erskine et al., 2006).

Table 2 - Error statistics at the Boulder runway

Metric	Slope	Aspect
Residuals below simulated error (%)	75	75
Average simulated uncertainty (°)	0.6	26.3
Mean observed error (°)	0.5	23.8
Max observed error (°)	45.8	180
Min observed error (°)	0.0	0.0

Uncertainty analysis using this approach were often performed with only knowledge of a single RMSE value for the entire DEM, and without direct knowledge of the spatial auto-correlation parameters necessary to describe spatial pattern of error in the DEM. The assumptions in this approach were required because information relating to the sensors and processing methods of the DEM are often unknown to end-users (Wechsler & Kroll, 2006). Within NEON, there is direct access to the hardware and processing procedures, allowing rigorous error propagation techniques to be implemented from the system sensor component errors, avoiding assumptions about the state of error within the DTM.

Currently, point cloud uncertainty is propagated from LiDAR system component errors according to Goulden and Hopkinson (2010), and also described in RD[03]. As a result, knowledge of the spatial patterns of uncertainty can be retained and this information can be further propagated into the slope and aspect products. Such a procedure is demonstrated for a DTM over a small (~700 ha) watershed in Goulden et al. (2016), which implemented identical procedures for DTM, slope and aspect development (TIN interpolation method and Horn algorithm for slope and aspect creation), although with a lower point spacing of ~1 pt / m2 than the nominal point spacing achieved by NEON LiDAR acquisitions (~4 pts /m2). Also, in Goulden et al. (2016) no morphological averaging filter (see Section 4.2.1) had been applied to the DTM in pre-processing. Results from Goulden et al. (under review) showed that simulated uncertainty was ~0.6°-1.5° and ~2.7°-40° for 95% of the slope and aspect maps respectively.

A similar analysis to Goulden et al. (2016) was performed with data acquired with the NEON LiDAR sensor over the Boulder runway. One hundred DTMs were simulated by varying the vertical error component in the point cloud by randomly selecting a value from within a normal distribution with standard deviation equal to the vertical coordinate uncertainty. Subsequently, one hundred slope and aspect maps were created from the DTMs. The standard deviation of the resulting value for each individual cell in the slope and aspect maps were used to simulate the uncertainty (**Figure 4**). Results of the test case on the Boulder runway showed simulated uncertainty averaged ~0.6° and ~26.3° for slope and aspect respectively (**Table 2**, **Figure 4**). This agrees well, although is slightly lower, with previous results from Goulden et al. (2016). This is expected because the Goulden et al. (2016) study was applied to a natural environment, and was not restricted to a smooth, reflective, flat runway surface where error is generally lower.

High accuracy validation data also exists over the Boulder runway which allows 'validation' slope and aspect to be determined over the runway, and compared against the slope and aspect determined from the LiDAR observations. Validation data on the runway consisted of 593 high accuracy post-processed kinematic (PPK) GPS points collected over two days. Validated slope and aspect values were determined by creating a DTM of the runway surface using the GPS validation points and a TIN algorithm, and then applying the (Horn, 1981) algorithm to determine slope and aspect. Observed errors (residuals) were then found by differencing the slope and aspect maps determined from the GPS validation data and the slope and aspect maps determined from the original (non-simulated) LiDAR observations, and retaining the absolute value of the difference (**Figure 4**). Subsequently, the simulated uncertainty in the slope and aspect products is compared against the residuals. Results show a general agreement between residuals and simulated uncertainty values, with 75% of residuals falling below simulated uncertainty in both the slope and aspect maps (Table 2). Since simulated uncertainty is produced at standard confidence we should expect 68% of residuals to fall below simulated uncertainty values, indicating the simulated uncertainty values are reasonable, but slightly pessimistic.
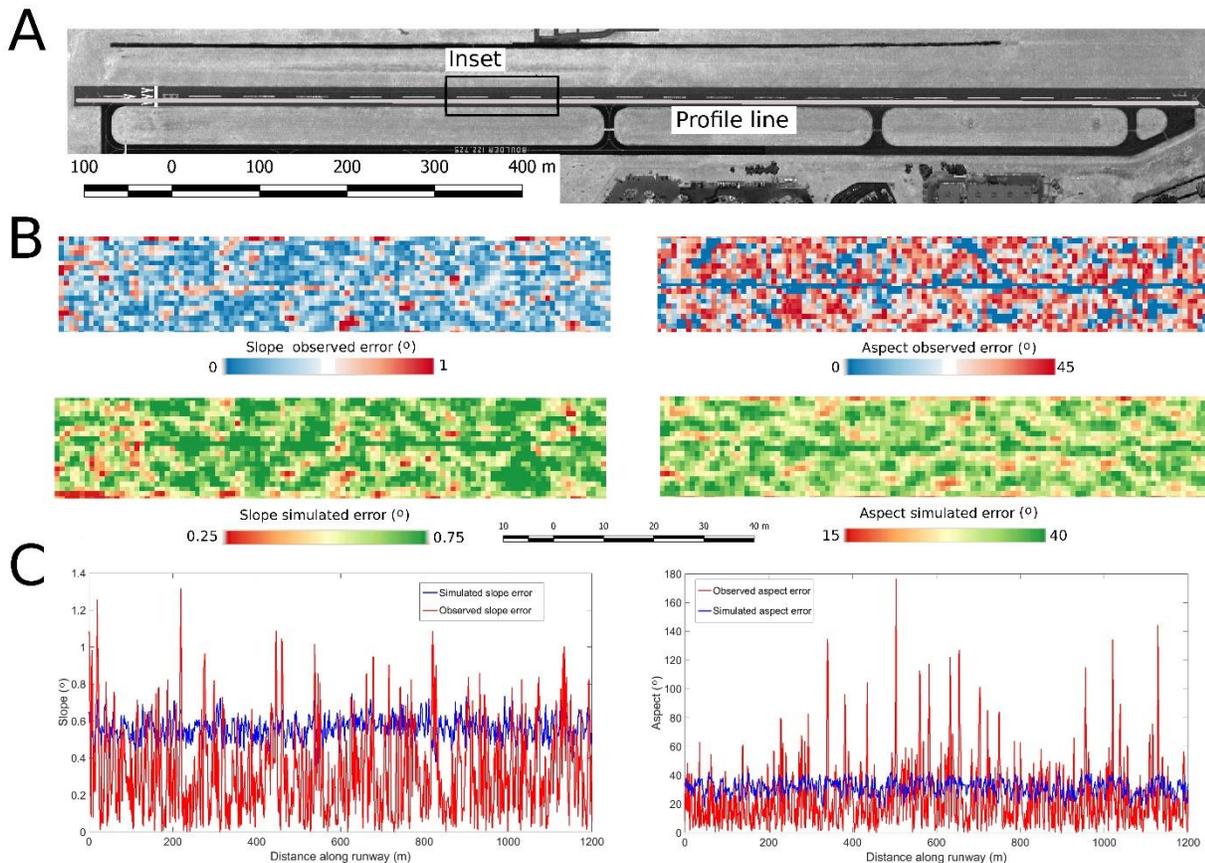
Figure 4 - Observed and simulated errors on the Boulder runway. Panel A: Intensity image of Boulder runway, panel B: observed and simulated errors for a portion of the runway, panel C: simulated and observed errors for a profile along the runway

6.2 Reported uncertainty

Currently, the Monte Carlo simulation approach described in Section 6.1 to quantify uncertainty for the slope and aspect products is not being generally applied. In the future, Monte Carlo simulations using modeled instrument errors for each individual point in the LiDAR point cloud will be implemented and rasters of slope and aspect uncertainty will be created and distributed with the slope and aspect products. Current results (Section 6.1) indicate that the uncertainty in slope and aspect is 0.6° and 26.3°, respectively on flat reflective surfaces (i.e. runway). It should be noted that although these results give a general impression of the level of error that can be expected, they cannot necessarily be extrapolated from the runway to natural environments where other error sources are known to contribute to the total error (i.e. terrain slope and vegetation). Furthermore, these results do not account for any uncertainty which falls into category two, or category 3, described in Section 6.

7 VALIDATION AND VERIFICATION

The algorithm used to produce the slope and aspect can be verified by comparison against results of industry standard software packages. To verify the algorithm, the ESRI ArcGIS software package was used to create slope and aspect maps from a section of the LiDAR survey of Talledega National Forest (TALL, **Figure 1**). ESRI software was selected for validation because ESRI also implements the Horn (1981) algorithm. Slope and aspect maps were created in ArcGIS and then differenced against the slope and aspect maps produced by the algorithm presented in the ATBD. Results showed that the differences between the slope and aspect maps produced by the NEON algorithm and by ArcGIS were negligible (**Figure 5**). The minor differences that did exist are likely the result of different machine rounding errors as the mean difference was essentially zero (< 0.005°) for both the slope and aspect.
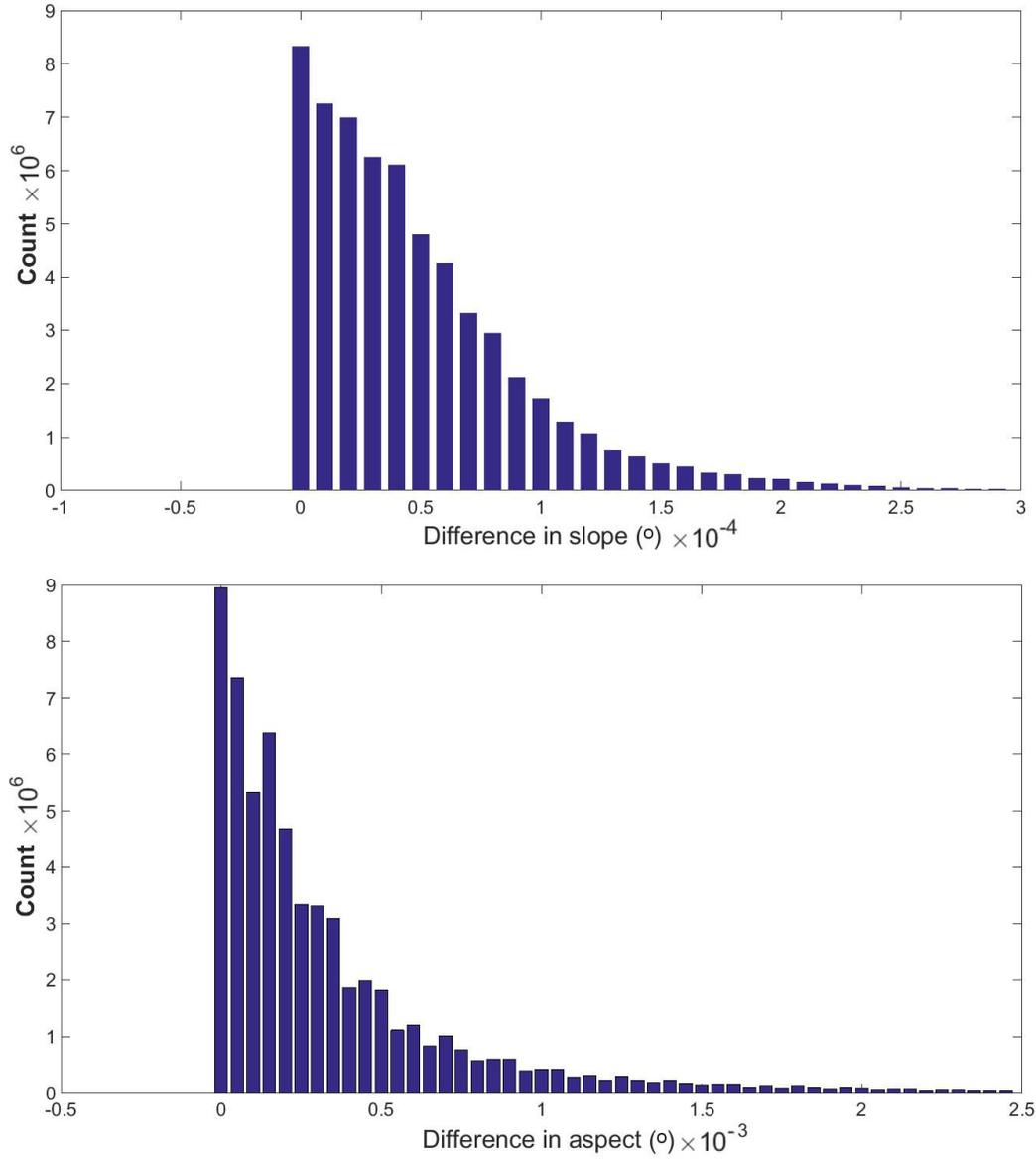
Figure 5 - Histograms of difference between slope and aspect produced by NEON and ESRI's ArcGIS Validation

8   FUTURE PLANS AND MODIFICATIONS

Future modifications to the slope and aspect product will be focused on developing a Monte Carlo simulation algorithm to produce raster maps of uncertainty in the slope and aspect product. Raster maps of uncertainty will be produced at 1 m of spatial resolution and also provided in geotiff / HDF5 format.

9   BIBLIOGRAPHY

Burrough, P. A. (1998). Principles of geographical information systems for land resources assessment. Oxford University Press, New York, NY.

Chang, K. & Tsai, B. (1991). The effect of dem resolution on slope and aspect mapping. Cartography and geographic information systems, 18(1), 69–77.

Erskine, R. H., Green, T. R., Ramirez, J. A., & MacDonald, L. H. (2006). Comparison of grid-based algorithms for computing upslope contributing area. Water Resources Research, 42(9).

ESRI. (2015, September 15). How aspect works. Retrieved from http://webhelp.esri.com/arcgisdesktop/9.2/index.cfm?TopicName=How%20Aspect%20works

Fisher, P. F. & Tate, N. J. (2006). Causes and consequences of error in digital elevation models. Progress in Physical Geography, 30(4), 467–489.

Florinsky, I. V. (1998). Accuracy of local topographic variables derived from digital elevation models. International Journal of Geographical Information Science, 12(1), 47–62.

Gates, D. M. (2012). Biophysical ecology. Courier Corporation.

Goulden, T., Hopkinson, C., Jamieson, R., & Sterling, S. (2014). Sensitivity of watershed attributes to spatial resolution and interpolation method of lidar dems in three distinct landscapes. Water Resources Research, 50(3), 1908–1927.

Goulden, T., Jamieson, R., Hopkinson, C., Sterling, S., Sinclair, A., & Hebb, D. (2014). Sensitivity of hydrological outputs from swat to dem spatial resolution. Photogrammetric Engineering & Remote Sensing, 80(7), 639–652.

Goulden, T. J., Hopkinson, C., Jamieson, R., & Sterling, S. (2016). Sensitivity of dem, slope, aspect and watershed attributes to lidar measurement uncertainty. Remote Sensing of Environment, 179, 23:35

Goulden, T. & Hopkinson, C. (2010). The forward propagation of integrated system component errors within airborne lidar data. Photogrammetric Engineering & Remote Sensing, 76(5), 589–601.

Holmes, K., Chadwick, O., & Kyriakidis, P. C. (2000). Error in a usgs 30-meter digital elevation model and its impact on terrain modeling. Journal of Hydrology, 233(1), 154–173.

Hopkinson, C., Chasmer, L., Munro, S., & Demuth, M. N. (2010). The influence of dem resolution on simulated solar radiation-induced glacier melt. Hydrological processes, 24(6), 775–788.

Horn, B. K. (1981). Hill shading and the reflectance map. Proceedings of the IEEE, 69(1), 14–47.

Hunter, G. J. & Goodchild, M. F. (1996). Communicating uncertainty in spatial databases. Transactions in GIS, 1(1), 13– 24.

Hunter, G. J. & Goodchild, M. F. (1997). Modeling the uncertainty of slope and aspect estimates derived from spatial databases. Geographical Analysis, 29(1), 35–49.

Hutchinson, M. F. & Gallant, J. C. (2000). Digital elevation models and representation of terrain shape. Terrain analysis: principles and applications, 29–50.

Jenson, S. K. & Domingue, J. O. (1988). Extracting topographic structure from digital elevation data for geographic information system analysis. Photogrammetric engineering and remote sensing, 54(11), 1593–1600.

Jones, K. H. (1998). A comparison of algorithms used to compute hill slope as a property of the dem. Computers & Geosciences, 24(4), 315–323.

Kienzle, S. (2004). The effect of dem raster resolution on first order, second order and compound terrain derivatives. Transactions in GIS, 8(1), 83–111.

McMaster, K. J. (2002). Effects of digital elevation model resolution on derived stream network positions. Water Resources Research, 38(4), 13–1.

Moore, I. D., Turner, A. K., Wilson, J. P., Jenson, S. K., & Band, L. E. (1993). Gis and land-surface-subsurface modeling. In M. Goodchild, B. Parks, & L. Steyaert (Eds.), Environmental modeling with gis (pp. 196–230). Oxford University Press, Inc.

Oksanen, J. & Sarjakoski, T. (2005). Error propagation of dem-based surface derivatives. Computers & Geosciences, 31(8), 1015–1027.

Quinn, P., Beven, K., Chevallier, P., & Planchon, O. (1991). The prediction of hillslope flow paths for distributed hydro- logical modelling using digital terrain models. Hydrological Processes, 5(1), 59–79. doi:10.1002/hyp.3360050106

Raaflaub, L. D. & Collins, M. J. (2006). The effect of error in gridded digital elevation models on the estimation of topographic parameters. Environmental Modelling & Software, 21(5), 710–732.

Ritter, N., Ruth, M., Grissom, B. B., Galang, G., Haller, J., Stephenson, G., …, Stickley, J., et al. (2000). Geotiff format specification geotiff revision 1.0. URL: http://www. remotesensing. org/geotiff/spec/geotiïome. html.

Skidmore, A. K. (1989). A comparison of techniques for calculating gradient and aspect from a gridded digital elevation model. International Journal of Geographical Information System, 3(4), 323–334.

Warren, S., Hohmann, M., Auerswald, K., & Mitasova, H. (2004). An evaluation of methods to determine slope using digital elevation data. Catena, 58(3), 215–233.

Wechsler, S. P. & Kroll, C. N. (2006). Quantifying dem uncertainty and its effect on topographic parameters. Photogrammetric Engineering & Remote Sensing, 72(9), 1081–1090.

Zevenbergen, L. W. & Thorne, C. R. (1987). Quantitative analysis of land surface topography. Earth surface processes and landforms, 12(1), 47–56.

Zhang, W. & Montgomery, D. R. (1994). Digital elevation model grid size, landscape representation. Water Resources Research, 30(4), 101.